SCIENTIFIC REPORTS

OPEN

SUBJECT AREAS:
MICROSCOPY
IMAGING

Received
11 August 2014

Accepted
18 December 2014

Published
4 February 2015

Correspondence and requests for materials should be addressed to T.I. (tali.ilovitsh@gmail.com)

* These authors contributed equally to this work.

Cellular imaging using temporally flickering nanoparticles

Tali Ilovitsh[1,2]*, Yossef Danan[1,2]*, Rinat Meir[1,2], Amihai Meiri[3] & Zeev Zalevsky[1,2]

[1]Faculty of Engineering, Bar Ilan University, Ramat-Gan 5290002, Israel, [2]The Bar-Ilan Institute of Nanotechnology & Advanced Materials, Bar Ilan University, Ramat-Gan 5290002, Israel, [3]Department of Electrical and Computer Engineering, University of Utah, Salt Lake City, Utah, USA.

Utilizing the surface plasmon resonance effect in gold nanoparticles enables their use as contrast agents in a variety of applications for compound cellular imaging. However, most techniques suffer from poor signal to noise ratio (SNR) statistics due to high shot noise that is associated with low photon count in addition to high background noise. We demonstrate an effective way to improve the SNR, in particular when the inspected signal is indistinguishable in the given noisy environment. We excite the temporal flickering of the scattered light from gold nanoparticle that labels a biological sample. By preforming temporal spectral analysis of the received spatial image and by inspecting the proper spectral component corresponding to the modulation frequency, we separate the signal from the wide spread spectral noise (lock-in amplification).

The ability to observe structures that are on a nanometric scale is a key merit for understanding cellular functions and design effective therapies for medical applications. Fluorescence microscopy was extensively used in the past in diffraction limited modalities as well as super resolution techniques. In all of these, fluorescent dyes and fluorescent proteins (FPs) are used as biomarkers[1–4]. However, typical drawbacks of fluorescence imaging methods are autofluorescence of live cells, the photo toxicity of FPs to living organisms and photobleaching[5–9]. Recently, numerous groups have demonstrated the use of gold nanoparticles (GNPs) as biomarkers[10–14] in a variety of biological applications such as biochemical sensing and detection[15], medical diagnostics[16], drug or gene delivery[17], nanoscopy[18], and therapeutic applications[19,20]. Their synthesis[21], conjugation[22], and assembly[23], is well known, making them inexpensive and easy to produce. Additional important attributes are their photostability, chemical stability and biocompatibility[24].

Surface Plamon Resonance (SPR) in GNPs results in high scattering and absorption cross sections, as well as spectral sensitivity, which make them attractive as biomarkers for imaging purposes. Under optical illumination at a wavelength that matches the surface electrons resonance, a strong amplification of the optical absorption and scattering will occur[25], where the resonance wavelength depends on the shape, dimensions and refractive index of the nanoparticle and the environment[24,25].

The effectiveness of nanoparticles as contrast agents depends on their optical properties[37]. For instance, a high scattering cross-section is essential for cell and biomedical imaging applications based on light scattering. On the other hand, applications using light absorption require a high nanoparticle absorption cross-section along with low scattering losses.

The use of GNPs as contrast agents improves the sensitivity and diagnostic ability of the imaging modality by site-specifically labeling tissues, cells or areas within a cell of interest. The effectiveness of nanoparticles as biomedical imaging contrast agents depends on their optical properties as well as the imaging system and the environmental conditions[26]. The size and shape of the GNP also affect the SPR efficiency[27,28]. A *20 nm* GNP has a high absorption with negligible scattering and therefore is suited to applications that use light absorption, whereas larger GNPs, for example, an *80 nm* GNPs, are more suitable for light-scattering-based imaging applications. Due to the high absorption cross section, heat is generated as a result of light absorption, which in the vicinity or a biological sample, can cause damage to the sample[29]. This sets a restriction on the laser intensity, thereby increasing the shot noise. For an aberration-free imaging system, the measured intensity of the image is given by the acquired data together with photon shot-noise, background noise, sensor's readout noise and dark current[30]. Therefore, of utmost importance in any imaging system, in particular one that is used for biomedical applications, is the ability to extract the data from the image even in poor SNR[31].

Various imaging methods measure the scattering from GNPs when tagging a biological sample. These include dark-field illumination[32], differential interference contrast and video enhancement[33], and total internal reflection[34]. However, the scattering is proportional to the sixth power of diameter which makes use of small

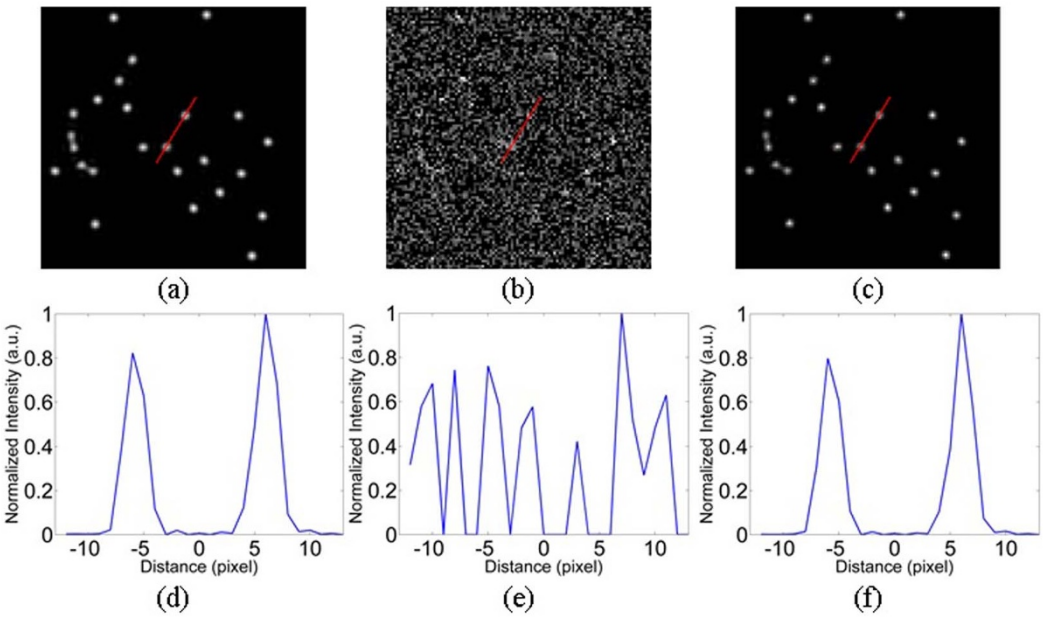

Figure 1 | Simulation results. (a) The simulated sample with random diffraction limited GNPs. (b) The image with added noise so that the SNR was -15 *dB*. (c) The image after applying the TSL technique, the SNR of the reconstructed image is *29 dB*. (d), (e) and (f) show the cross section of the dashed red line that passes through the center of an emitter in the middle part of the image of (a), (b) and (c) respectively.

nanoparticle difficult. They also must be discriminated from a strong background noise, especially if the particles are to be detected in cells or tissues, which leads to a low SNR. Other methods are based on the photothermal effect, *i.e.* a change in temperature around the particle when incident laser light is absorbed by the nanoparticle. The temperature change leads to a local variation in the index of refraction, which is translated into a detectable phase change[35–40]. Recent studies showed photothermal imaging in wide-field mode[40], lock-in detection[36] or combination of both[35], however they require a complex setup and high laser intensity.

The method demonstrated in this paper is based on the lock-in amplification technique which involves temporally sequenced labeling (TSL) as an imaging tool. TSL can suppress image noise and recover the data by using a tradeoff between the time of measurement and improved SNR with low laser intensity and a simple optical setup[41,42]. Lock-in amplification is a widely used technique, for example in measurement of atomic emission[43], absorption[44], and fluorescence spectrometry[45]. The advantages of the method are its ability to measure very low-light levels (high sensitivity), its relative insensitivity to changes in detector gain, and its ability to discriminate data from the image noise. The method is based on the fact that even when noise and signal are indistinguishable in the time domain, if the signal has a definite frequency band and there is no large noise peak within that band, noise and signal can be sufficiently separated via usage of the frequency domain.

In TSL we modulate a laser beam at a wavelength that matches the GNPs SPR, with a known periodic flickering at temporal frequency of f_0. A temporal sequence of intensity images of light scattered from the sample that contains GNPs is captured. The intensity of each image is proportional to the sum of a time sample of the modulated signal and the additive noise:

$$I_t(f) = I_{sig_t}(f_0) + I_{noise_t}(f), \tag{1}$$

where I_t is the image intensity, I_{sig} is the signal intensity without noise, I_{noise} is the noise intensity and $t=1.....N$ is the index of each image, where N is the number of images that were captured. Due to

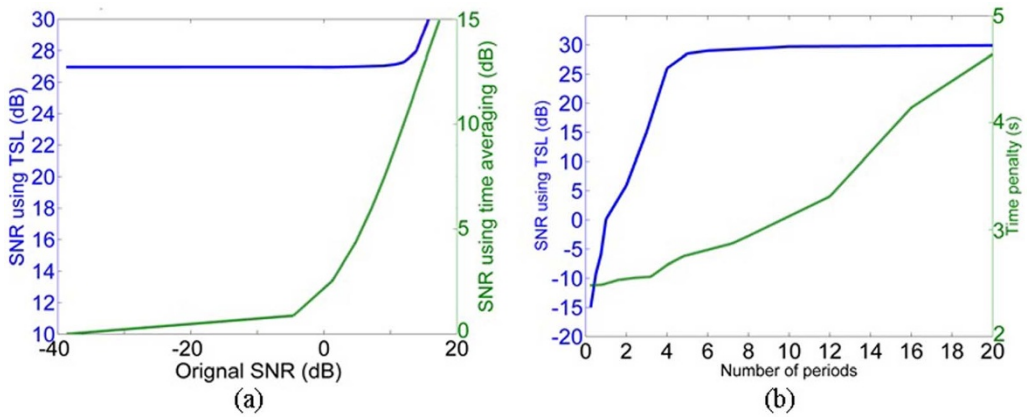

Figure 2 | Summary of the obtained simulation results. (a) x-axis is the SNR of the original image. left y-axis is the SNR after preforming the TSL and the right y-axis is the SNR after preforming time averaging. (b) Left y-axis is the effect of the number of periods of the modulation signal that is required for achieving maximum improvement in the SNR. Right y-axis is the additional computer processing time as a function of the number of periods, with modulation frequency of *3 Hz* and image capturing frame rate of *12 Hz*.

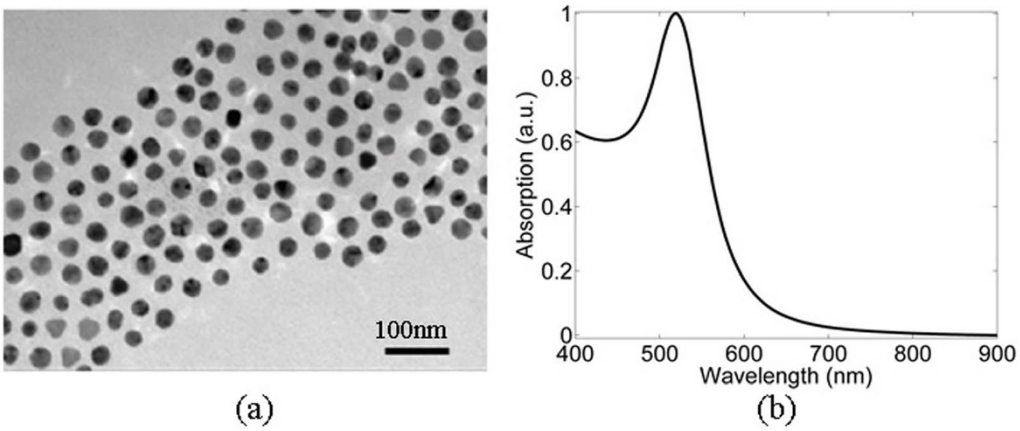

Figure 3 | characterization of GNPs. (a) TEM image of *20 nm* GNPs. (b) Ultraviolet-visible spectroscopy of the GNPs.

the modulations, the signal components are expected to be around the modulation frequency, whereas the noise is spread over a wider spectrum, a fact that allows the reconstruction of the signal after post processing. The post processing is done using MATLAB (MathWorks, Natick, MA, USA).

After recording the sequence of images, each image is convolved with the modulation signal

$$I_{conv_t} = I_t(f) * I_{mod_t}(f_0), \tag{2}$$

where I_{mod} is the intensity of the modulation signal and I_{conv} is the result of the convolution. The reconstructed image is the average sum of all the images:

$$I_{TSL} = \frac{1}{N}\sum_{t=1}^{N} I_{conv_t} \tag{3}$$

After the convolution, the contribution from any signal that is not at the same temporal frequency as the modulation signal (i.e. the noise), is attenuated close to zero, while the image data is recovered.

Simulations

To evaluate the performance of the method and its impact on the SNR, Monte-Carlo simulations were used to generate mock data sets with random emitters in each set. In these simulations the model was of a sample that contains GNPs with peak emission at wavelength of λ=*532 nm*. The sample was illuminated using temporally modulated laser at λ=*532 nm*. The object was imaged through an objective lens onto a Complementary-Metal-Oxide-Semiconductor (CMOS) camera. Background noise was introduced by adding a sample from a Poisson distribution random variable with variance N_b (assumed constant across the field of view), and shot noise was introduced by sampling a Poisson random process with an expected value which corresponds to the noiseless pixel values[46].

A sequence of time dependent images was generated and analyzed. The SNR, the modulation frequency and the number of frames were all allowed to vary. Using the a priori knowledge of the temporal modulation frequency, the images were convolved with the modulation signal followed by time averaging to result in an improved SNR. The result was compared to a simple time averaging of the images for the same time period. As an example, Figure 1(a) shows a simulated sample with random diffraction limited spots originating from scattering from the GNPs. Noise was added to the image, corresponding to SNR of −15 dB, see Figure 1(b), where after applying TSL, the SNR improved to 29 dB, as shown in Figure 1(c). Figure 1(d), (e) and (f) show the cross section of the dashed red line along the axis connecting two emitters in the middle part of the image of (a), (b) and (c) respectively.

In conventional methods, post processing using de-convolution algorithms can improve the performance and the SNR[47]. However in order to apply them one needs to have images where the particles are seen. Since the set of images used here are so noisy that the particles are indistinguishable, these methods are not applicable here. The SNR of the original image with the added noise was calculated by

$$SNR_{or} = 10\log_{10}\sqrt{\frac{\frac{1}{N}\sum_{i=1}^{N} {I_{sig_i}}^2}{\frac{1}{N}\sum_{i=1}^{N} {I_{noise_i}}^2}} \tag{4}$$

After applying the proposed technique, the obtained SNR is:

$$SNR_{TSL} = 10\log_{10}\sqrt{\frac{\frac{1}{N}\sum_{i=1}^{N} {I_{conv_i}}^2}{\frac{1}{N}\sum_{i=1}^{N} (I_{conv_i} - I_i)^2}} \tag{5}$$

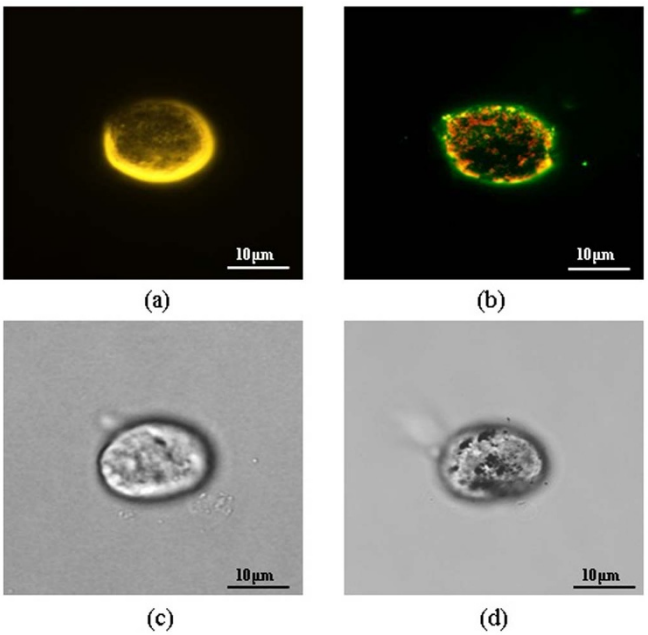

Figure 4 | Comparison of a sample that contained GNP tagged cells and a control sample that contained only cells. (a) and (b) are dark-field microscopy images of both the control and the GNP tagged cell, respectively. (c) and (d) are the confocal microscopy images of these two samples, at depth of 4 μm into the cell.

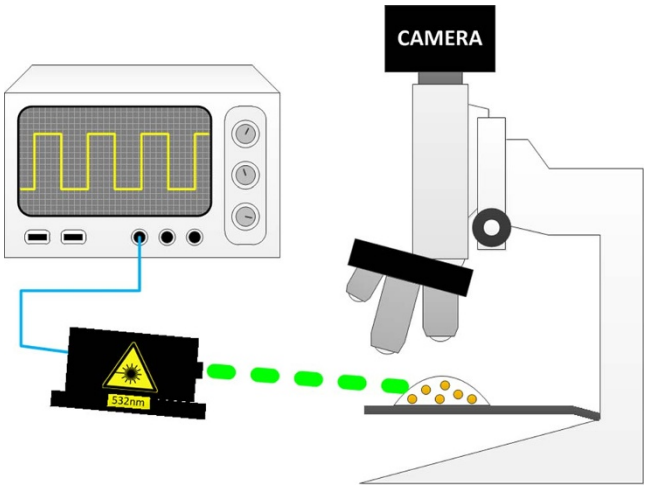

Figure 5 | The experimental setup is composed of a function generator that modulates a green laser at wavelength of 532 nm. The modulated beam illuminated the sample and the scattered light as a function of time was imaged using the Olympus BX51 microscope with a 40x objective lens and recorded with the CMOS camera (PixeLink PLA741E).

As can be seen in Figure 2(a) that by using TSL, the SNR improvement is the highest at low SNRs and that the method can reconstruct the signal even when the signal is almost indistinguishable before applying the proposed approach. When comparing the obtained results to simple time averaging, at low SNRs, the TSL performance is significantly higher and can reach an improvement of >25 dB. When the SNR of the original image is increased, the difference in the performance of both methods is reduced as expected.

Another important factor is the time penalty that the method invokes. This penalty stems from the need to collect a sufficient number of images of the modulated sample as a function of time. The performance of TSL as a function of the number of modulation signal periods ($T=1/f_0$), and time penalty are presented in Figure 2(b). In these simulations the original SNR was -15 *dB*. For total integration time which corresponds to less than 1 period, the effect was negligible. When the integration time increases, the SNR improves considerably, reaching a value of ~ 30 *dB*, for 6 periods. Increasing the integration time to more than 6 periods did not have further effect on the SNR. For the analysis of the additional computer processing time (time penalty) as a function of the number of periods, we used a frame rate of *12 frames/s* and $f_0=3$ *Hz* to match those of our experimental setup. We see in Figure 2(b) that the time penalty for 6 periods is ~ 2.8 seconds using a simple PC (HP Compaq Elite 8300 Microtower PC with Windows 7 professional 64 bit operation system, Intel® Core™ i5-3470 processor, *3.20 GHz*, *12 GB* RAM). Increasing the frame rate to 24 frames per second and modulation frequency to 6 Hz will decrease the time penalty to 1.4 seconds. The frame rate in this case is limited by the exposure time, which is determined by the camera sensitivity, laser intensity and the scattering cross section of the nanoparticles.

Experimental Results

For the experiments we used live Mouse melanoma cells (B16)[48] that were injected with *20 nm* GNPs with a peak absorption at *532 nm* immobilized on a coverslip using a well-established procedure[49–51] (the sample preparation is described in the methods section below). A protective layer of PEG was absorbed on the surface of the GNPs followed with their coating with glucose in order to increase cell-uptake rate and stability. Particle size, shape, and uniformity were measured using transmission electron microscopy (TEM) and verified to be 20 *nm* diameter spheres (Figure 3 (a)). Their absorption spectrum is shown in Figure 3 (b), which presents a clear peak absorption at *532 nm* as expected.

In order to confirm the existence of GNPs on the cell membrane and internalized into cell, two samples were made. One contained GNP tagged cells and a control sample that contained only cells. Both samples were imaged using a dark-field microscope (Nikon i50), as shown in Figure 4 (a) and (b), for the control sample and GNP tagged cells, respectively. The scattered light from the control experiment has a wide spectrum, making the cells without GNPs appear yellow (Figure 4(a)). The scattered light from the GNPs has a peak around *532 nm*, which make them appear green. High density regions appear red due to the plasmon coupling[52]. This is clearly seen in Figure 4(b), which proof the existence of GNPs in the sample.

In order to confirm the existence of GNPs within the cells and on the cell membrane, a Z axis scan of the sample using a confocal microscope (Leica TCS SP5) was performed on both samples. The thickness of the sample was measured to be *13* μm, and the scan was done using steps of *0.8* μm. Figure 4 (c) and (d) show the images of a cell that contains GNPs and a control cell without GNPs, respectively, at depth of *4* μm into the cells. In Figure 4 (d) there are a lot of small dark spots, which do not exist in the control (Figure 4(c)), and therefore are the GNPs. The GNPs entered the cell, however weren't targeted into a specific area within a cell and therefore are randomly distributed[53]. They can also enter a specific organelle or area within the cell, and high concentration zones are seen as clusters of GNPs. In addition there are also other organelles that can be seen (and can also be seen in the control image).

For the TSL experiments, a function generator (AFG3022B by Tektronix) was used to create a square wave with a known frequency of 3 Hz (that fulfils the Nyquist sampling criteria as the frame rate of the camera was *12 frames/s*), and a duty cycle of *50%*. This signal modulated a green laser at *532 nm* (Photop DPGL-2100F), which illuminated the sample. The scattered light as a function of time was imaged using the Olympus BX51 microscope with a *40x* objective lens and recorded with the CMOS camera (PixeLink PL-A741-E). The experimental setup is described in Figure 5.

The effective pixel size was *167.5 nm* and the camera was set to a gain of *17.7 dB* and exposure time of *20 ms*. The laser power was set to *8 mW* to mimic high background and shot noise conditions, where the SNR of the original image was calculated to be *-25 dB*.

Figure 6 presents a sequence of recorded images of the scattered light from the sample with -25 *dB* SNR. The presented images were captured every *20 msec*. It is clearly seen that the signal is almost indistinguishable. The Fourier transform of the temporal fluctuations of the pixels in the images is presented in Figure 7. When observing the Fourier transform of a data pixel, a clear peak is visible at the modulation frequency of *3 Hz* (red line) while the Fourier transform of a noise pixel does not contain any peak (black line).

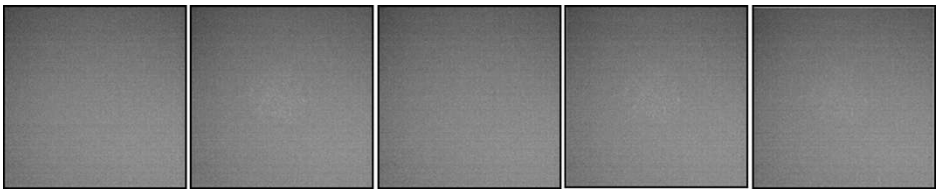

Figure 6 | Sequence of recorded images of the scattered light from the sample having −25 dB SNR. The irradiation was using a laser beam (at 532 nm) that was modulated using modulation frequency of 3 Hz. The presented images were captured every 20 msec.

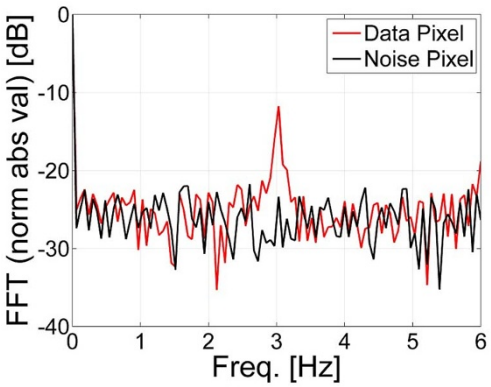

Figure 7 | The Fourier transform of the temporal fluctuations of pixels in the recorded images. The data pixels present a clear peak at the modulation frequency of 3 Hz (red line) and the noise pixel does not contain any peak (black line).

A bright field image of the sample can be seen in Figure 8(a). The TSL technique was applied to the sequence of recorded images and the result was a clear image of the GNPs in the observed sample (Figure 8(b)). In order to verify the results, a reference image using *0 dB* gain, exposure time of *130 ms* and a continuous wave laser illumination was taken, and is shown in Figure 8(c). The similarity between Figure 8(b) and Figure 8(c) is clearly visible, which means that the reconstructed image using TSL contains the scattering signal from the GNPs in the sample. Figure 8(d) is the superimposing of Figure 8(a) and Figure 8(b), where the GNPs are marked in red. There is an overlap between the locations of the GNPs to that of the cells which indicate that the GNPs are concentrated inside the cells, and by using the ability to attach the GNPs to a specific area within a cell, the proposed technique provides a tool intra-cellular processes study.

The experiments were performed using *532 nm* laser source. When preforming cellular imaging at short wavelengths, the intra-cellular matter (vesicles and fragment) also afford the noise[54]. A further improvement of the SNR can be obtained by working at longer wavelength, such as Near Infra-Red. The proposed technique is applicable at all wavelengths, given GNPs with peak absorption that matches the laser wavelength.

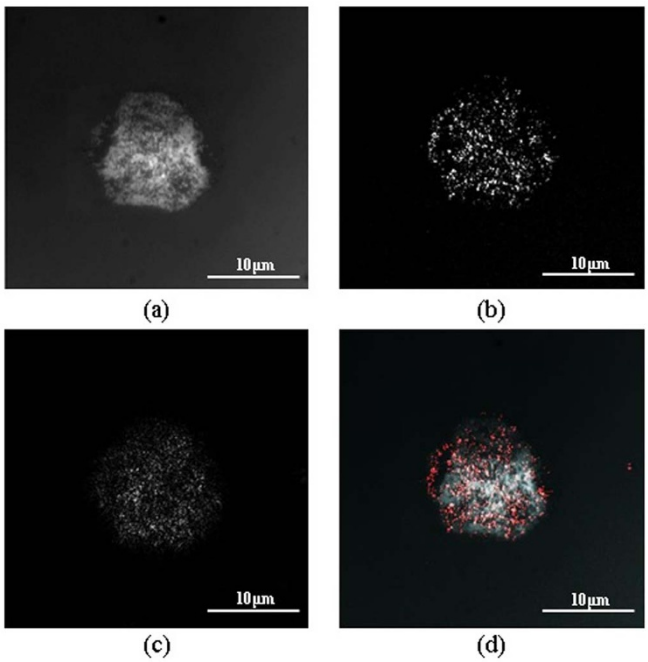

Figure 8 | Expeirmentally extracted images. (a)A bright field image of the sample. (b) The reconstructed image of the sample using TSL. (c) A reference image of the sample with high SNR and high laser intensity. (d) The superimposing of (a) and (b), where the GNPs are marked in red.

Methods

Materials. *GNPs Synthesis.* GNPs were prepared using sodium citrate according to the known methodology described by Enustun and Turkevic[55]. 0.414 mL of 1.4 M $HAuCl_4$ solution in 200 mL water was added to a 250 mL single-neck round bottom flask and stirred in an oil bath on a hot plate until boiled. 4.04 mL of a 10% sodium citrate solution (0.39 M sodium citrate tribasic dihydrate 98%, Sigma cas 6132-04-3) was then quickly added. The solution was stirred for 5 min, and then the flask was removed from the hot oil and placed aside until cooled.

GNPs Conjugation. In order to prevent aggregation and to stabilize the particles in physiological solutions, *O*-(2-Carboxyethyl)-*O′*-(2-mercaptoethyl)heptaethylene glycol (PEG7) (95%, Sigma-Aldrich, Israel Ltd.) was absorbed onto the GNPs. This layer also provides the chemical groups required for conjugation (-COOH). First, the solution was centrifuged to dispose of excess citrate. PEG7 solution was then added to the GNP solution, stirred overnight and put in a centrifuge in order to dispose of excess PEG. In order to increase cell-uptake rate, stabilized GNPs were further coated with glucose. Excess EDC (N-ethyl-N-(3-dimethylaminopropyl) carbodiimide) and NHS (N-hydroxysuccinimide) (Thermo Fisher Scientific, Inc, Rockford, IL) were added to the solution, followed by addition of Glucose-2 (2GF)(D-(+)-Glucosamine hydrochloride, Sigma-Aldrich, Israel Ltd.). NHS and EDC form an active ester intermediate with the -COOH functional groups, which can then undergo an amidation reaction with the glucose $-NH_2$ group.

Cell uploading with GNP. A431 cells were cultured in 5 ml glucose-free DMEM medium containing 5% FCS, 0.5% Penicillin and 0.5% glutamine. Cells were centrifuged and a saline solution containing GNPs was added in excess. The cells were then incubated at 37°C for 1 hour. After incubation, the cells were centrifuged twice (7 minutes in 1000 rpm) to wash out unbound nanoparticles.

Fixation (used for confocal microscopy). GNP-labeled-cells were incubated in Formaldehyde solution at room temperature.

1. Lichtman, J. W. & Conchello, J. Fluorescence microscopy. *Nat. Metho* **2**, 910–919 (2005).
2. Denk, W., Strickler, J. & Webb, W. Two-photon laser scanning fluorescence microscopy. *Science (80-.).* **52**, 1778–9 (1990).
3. Huang, B., Bates, M. & Zhuang, X. Super resolution fluorescence microscopy. *Annu. Rev. Biochem.* **78**, 993–1016 (2009).
4. Resch-Genger, U. & Grabolle, M. Quantum dots versus organic dyes as fluorescent labels. *Nat. Methods* **5**, 763–775 (2008).
5. Mansfield, J. Autofluorescence removal, multiplexing, and automated analysis methods for in-vivo fluorescence imaging. *J. Biomed. Opt.* **10**, 41207 (2005).
6. Hoebe, R. & Oven, C. Van. Controlled light-exposure microscopy reduces photobleaching and phototoxicity in fluorescence live-cell imaging. *Nat. Biotechnol.* **25**, 249–53 (2007).
7. Henderson, J., Ai, H. W., Campbell, R. E. & Remington, S. J. Structural basis for reversible photobleaching of a green fluorescent protein homologue. *Proc. Natl. Acad. Sci. U. S. A.* **104**, 6672–7 (2007).
8. Bernas, T., Zarebski, M., Cook, R. R. & Dobrucki, J. W. Minimizing photobleaching during confocal microscopy of fluorescent probes bound to chromatin: role of anoxia and photon flux. *J. Microsc.* **215**, 281–96 (2004).
9. Carpentier, P., Violot, S., Blanchoin, L. & Bourgeois, D. Structural basis for the phototoxicity of the fluorescent protein KillerRed. *FEBS Lett.* **583**, 2839–42 (2009).
10. Murphy, C. *et al.* Gold nanoparticles in biology: beyond toxicity to cellular imaging. *Acc. Chem. Res.* **41**, 1721–30 (2008).
11. Wilson, R. The use of gold nanoparticles in diagnostics and detection. *Chem. Soc. Rev.* **37**, 2028–45 (2008).
12. Ankri, R., Duadi, H., Motiei, M. & Fixler, D. In-vivo Tumor detection using diffusion reflection measurements of targeted gold nanorods - a quantitative study. *J. Biophotonics* **5**, 263–73 (2012).
13. Salem, A., Searson, P. & Leong, K. Multifunctional nanorods for gene delivery. *Nat. Mater.* **2**, 668–71 (2003).
14. Hirsch, L. R. *et al.* Nanoshell-mediated near-infrared thermal therapy of tumors under magnetic resonance guidance. *Proc. Natl. Acad. Sci. U. S. A.* **100**, 13549–54 (2003).
15. Polak, P., Zalevsky, Z. & Shefi, O. Gold nanoparticles-based biosensing of single nucleotide DNA mutations. *Int. J. Biol. Macromol.* **59**, 134–7 (2013).
16. Fixler, D. & Zalevsky, Z. In Vivo Tumor Detection Using Polarization and Wavelength Reflection Characteristics of Gold Nanorods. *Nano Lett.* **13**, 6292–6296 (2013).

17. Truong, P. L., Kim, B. W. & Sim, S. J. Rational aspect ratio and suitable antibody coverage of gold nanorod for ultra-sensitive detection of a cancer biomarker. *Lab Chip* **12**, 1102–9 (2012).
18. Gur, A., Fixler, D., Micó, V., Garcia, J. & Zalevsky, Z. Linear optics based nanoscopy. *Opt. Express* **18**, 22222–31 (2010).
19. Zhan, Q., Qian, J., Li, X. & He, S. A study of mesoporous silica-encapsulated gold nanorods as enhanced light scattering probes for cancer cell imaging. *Nanotechnology* **21**, 055704 (2010).
20. Ankri, R. *et al.* Intercoupling surface plasmon resonance and diffusion reflection measurements for real-time cancer detection. *J. Biophotonics* **6**, 188–96 (2013).
21. Yokota, S., Kitaoka, T., Opietnik, M., Rosenau, T. & Wariishi, H. Synthesis of gold nanoparticles for in situ conjugation with structural carbohydrates. *Angew. Chem. Int. Ed. Engl.* **47**, 9866–9 (2008).
22. El-Sayed, I. H., Huang, X. & El-Sayed, M. A. Surface plasmon resonance scattering and absorption of anti-EGFR antibody conjugated gold nanoparticles in cancer diagnostics: applications in oral cancer. *Nano Lett.* **5**, 829–34 (2005).
23. Yang, P.-H., Sun, X., Chiu, J.-F., Sun, H. & He, Q.-Y. Transferrin-mediated gold nanoparticle cellular uptake. *Bioconjug. Chem.* **16**, 494–6 (2005).
24. Shukla, R. *et al.* Biocompatibility of gold nanoparticles and their endocytotic fate inside the cellular compartment: a microscopic overview. *Langmuir* **21**, 10644–54 (2005).
25. Seekell, K., Price, H., Marinakos, S. & Wax, A. Optimization of immunolabeled plasmonic nanoparticles for cell surface receptor analysis. *Methods* **56**, 310–6 (2012).
26. Fong, W. K., Hanley, T. L., Thierry, B., Kirby, N. & Boyd, B. J. Plasmonic nanorods provide reversible control over nanostructure of self-assembled drug delivery materials. *Langmuir* **26**, 6136–9 (2010).
27. Jain, P. K., Lee, K. S., El-Sayed, I. H. & El-Sayed, M. A. Calculated absorption and scattering properties of gold nanoparticles of different size, shape, and composition: applications in biological imaging and biomedicine. *J. Phys. Chem. B* **110**, 7238–48 (2006).
28. Kelly, K. & Coronado, E. The optical properties of metal nanoparticles: the influence of size, shape, and dielectric environment. *J. Phys. …* **107**, 668–677 (2003).
29. Qin, Z. & Bischof, J. C. Thermophysical and biological responses of gold nanoparticle laser heating. *Chem. Soc. Rev.* **41**, 1191–217 (2012).
30. Thompson, R. E., Larson, D. R. & Webb, W. W. Precise nanometer localization analysis for individual fluorescent probes. *Biophys. J.* **82**, 2775–83 (2002).
31. Tapiovaara, M. J. & Wagner, R. F. SNR and noise measurements for medical imaging: I. A practical approach based on statistical decision theory. *Phys. Med. Biol.* **38**, 71–92 (1993).
32. Schultz, S. & Smith, D. Single-target molecule detection with nonbleaching multicolor optical immunolabels. *Proc. Natl. Acad. Sci. U. S. A.* **97**, 996–1001 (2000).
33. Gelles, J., Schnapp, B. & Sheetz, M. Tracking kinesin-driven movements with nanometre-scale precision. *Nature* **331**, 450–453 (1988).
34. Sönnichsen, C. *et al.* Spectroscopy of single metallic nanoparticles using total internal reflection microscopy. *Appl. Phys. Lett.* **77**, 2949 (2000).
35. Eldridge, W. J., Meiri, A., Sheinfeld, A., Rinehart, M. T. & Wax, A. Fast wide-field photothermal and quantitative phase cell imaging with optical lock-in detection. *Biomed. Opt. Express* **5**, 2517 (2014).
36. Pache, C. *et al.* Fast three-dimensional imaging of gold nanoparticles in living cells with photothermal optical lock-in Optical Coherence Microscopy. *Opt. Express* **20**, 21385–99 (2012).
37. Berciaud, S., Lasne, D., Blab, G., Cognet, L. & Lounis, B. Photothermal heterodyne imaging of individual metallic nanoparticles: Theory versus experiment. *Phys. Rev. B* **4**, 045424 (2006).
38. Berciaud, S., Cognet, L., Blab, G. A. & Lounis, B. Photothermal heterodyne imaging of individual non-fluorescent nano-objects. *Phys. Rev. Lett.* **25**, 1–15 (2004).
39. Boyer, D., Tamarat, P., Maali, A., Lounis, B. & Orrit, M. Photothermal imaging of nanometer-sized metal particles among scatterers. *Science* **297**, 1160–3 (2002).
40. Turko, N. A., Peled, A. & Shaked, N. T. Wide-field interferometric phase microscopy with molecular specificity using plasmonic nanoparticles. *J. Biomed. Opt.* **18**, 111414 (2013).
41. Wolfson, R. The lock-in amplifier: A student experiment. *Am. J. Phys* **59**, 569–572 (1991).
42. Bhagyajyoti, J., Sudheer, L., Bhaskar, P. & Parvathi, C. Review on Lock-in Amplifier. *Int. J. Sci. Eng. Technol. Res.* **1**, 40–45 (2012).
43. Sonnaillon, M. O. & Bonetto, F. J. A low-cost, high-performance, digital signal processor-based lock-in amplifier capable of measuring multiple frequency sweeps simultaneously. *Rev. Sci. Instrum.* **76**, 024703 (2005).
44. Arnott, W. P., Moosmüller, H., Rogers, C. F., Jin, T. & Bruch, R. Photoacoustic spectrometer for measuring light absorption by aerosol: instrument description. *Atmos. Enviroment* **33**, 2845–2852 (1999).
45. Murphy, M. K., Clyburn, S. A. & Veillon, C. Comparison of lock-in amplification and photon counting with low background flames and graphite atomizers in atomic fluorescence spectrometry. *Anal. Chem.* **45**, 1468–1473 (1973).
46. Waters, J. C. Accuracy and precision in quantitative fluorescence microscopy. *J. Cell Biol.* **185**, 1135–48 (2009).
47. Sibarita, J. B. Deconvolution microscopy. *Adv. Biochem. Eng. Biotechnol.* **95**, 201–243 (2005).
48. Danciu, C. *et al.* A characterization of four B16 murine melanoma cell sublines molecular fingerprint and proliferation behavior. *Cancer Cell Int.* **13**, 75 (2013).
49. Reuveni, T., Motiei, M., Romman, Z., Popovtzer, A. & Popovtzer, R. Targeted gold nanoparticles enable molecular CT imaging of cancer: an in vivo study. *Int. J. Nanomedicine* **6**, 2859–2864 (2011).
50. Shilo, M., Motiei, M., Hana, P. & Popovtzer, R. Transport of nanoparticles through the blood-brain barrier for imaging and therapeutic applications. *Nanoscale* **6**, 2146–52 (2014).
51. Curry, T., Kopelman, R., Shilo, M. & Popovtzer, R. Multifunctional theranostic gold nanoparticles for targeted CT imaging and photothermal therapy. *Contrast Media Mol. Imaging* **9**, 53–61 (2014).
52. Jain, P. K., Eustis, S. & El-Sayed, M. a. Plasmon coupling in nanorod assemblies: optical absorption, discrete dipole approximation simulation, and exciton-coupling model. *J. Phys. Chem. B* **110**, 18243–53 (2006).
53. Dykman, L. A. & Khlebtsov, N. G. Uptake of engineered gold nanoparticles into mammalian cells. *Chem. Rev.* **114**, 1258–88 (2014).
54. Xiao, L., Wei, L., Cheng, X., He, Y. & Yeung, E. S. Noise-free dual-wavelength difference imaging of plasmonic resonant nanoparticles in living cells. *Anal. Chem.* **83**, 7340–7 (2011).
55. Enustun, B. & Turkevich, J. Coagulation of colloidal gold. *J. Am. Chem. Soc.* **85**, 3317–3328 (1963).

Author contributions

T.I. wrote the main manuscript text and R.M. wrote the materials and methods section. T.I. and Y.D. preformed the experiments. A.M. and Z.Z. advised the work. All authors reviewed the manuscript. All authors have given approval to the final version of the manuscript.

Additional information

Competing financial interests: The authors declare no competing financial interests.

How to cite this article: Ilovitsh, T., Danan, Y., Meir, R., Meiri, A. & Zalevsky, Z. Cellular imaging using temporally flickering nanoparticles. *Sci. Rep.* **5**, 8244; DOI:10.1038/srep08244 (2015).